Light-Front Transverse Nucleon Charge and Magnetisation Densities

Z.-N. Xu (徐珍妮)^{ID}, ¹ Z.-Q. Yao (姚照千) ^{ID}, ², * P. Cheng (程鹏) ^{ID}, ³ C. D. Roberts^{ID}, ⁴, ⁵, [†] J. Rodríguez-Quintero ^{ID}, ¹, [‡] and J. Segovia ^{ID6}

¹Dpto. Ciencias Integradas, Centro de Estudios Avanzados en Fis., Mat. y Comp.,
Fac. Ciencias Experimentales, Universidad de Huelva, E-21071 Huelva, Spain
 ²Helmholtz-Zentrum Dresden-Rossendorf, Bautzner Landstraße 400, D-01328 Dresden, Germany
 ³Department of Physics, Anhui Normal University, Wuhu, Anhui 24100, China
 ⁴School of Physics, Nanjing University, Nanjing, Jiangsu 210093, China
 ⁵Institute for Nonperturbative Physics, Nanjing University, Nanjing, Jiangsu 210093, China
 ⁶Dpto. Sistemas Físicos, Químicos y Naturales, Univ. Pablo de Olavide, E-41013 Sevilla, Spain (Dated: 2025 November 15)

Nucleon elastic electromagnetic form factors obtained using both the three-body and quark + fully-interacting-diquark pictures of nucleon structure are employed to calculate an array of light-front transverse densities for the proton and neutron and their dressed valence-quark constituents, viz. flavour separations of the proton and neutron results. These two complementary descriptions of nucleon structure deliver mutually compatible predictions, which match expectations based on modern parametrisations of available data, where such are available. Amongst other things, it is found that transverse-plane valence u- and d-quark Dirac radii are practically indistinguishable; but regarding kindred Pauli radii, the d quark value is roughly 10% greater than that of the u-quark. Moreover, magnetically, the valence d quark is far more active than the valence u quark, probably because it has much greater orbital angular momentum. Both pictures of nucleon structure agree in predicting that, in a polarised nucleon, the transverse-plane charge densities are no longer rotationally invariant. Instead, for a $+\hat{x}$ polarised nucleon, positive charge is displaced in the $-\hat{y}$ direction, with the opposite effect for negative charge.

I. INTRODUCTION

Drawing charts of nuclear and nucleon structure has long been a principal goal of high energy nuclear and particle physics. Focusing on nucleons, the Poincaré-invariant electromagnetic form factors contain much objective information. Recognising this, a great deal of electron + nucleon scattering data has been collected and analysed since the pioneering experiments described in Ref. [1]. That progress is canvassed in, e.g., Refs. [2–5].

Understanding and relating modern data to a sound picture of nucleon structure requires robust theory. Since the data now extend to large values of spacelike squared momentum transfer, viz. $0 < Q^2 \lesssim 15\,\mathrm{GeV}^2$ [6, 7], a coherent description requires a Poincaré-covariant approach because one is delving deep into a target with highly relativistic constituents.

One such scheme is provided by lattice-regularised quantum chromodynamics (lattice-QCD or lattice Schwinger function methods). Material progress has been made in developing lattice-QCD for form factor calculations since the turn of this century; see, e.g., Refs. [8–13]. Notwithstanding that, reaching the large- Q^2 domain now accessible to experiments remains difficult using lattice-QCD, owing to the need for very fine lattices and large volumes, and issues with signal-to-noise ratio and excited state contamination [13].

Hamiltonian-based light-front approaches and relativistic and/or holographic quark models have also been used [14–19] with some success. The issue in these cases, however, is forging a link to QCD because the degrees of freedom used to formulate the models do not have a traceable connection to those in the QCD action.

A viable alternative to the aforementioned approaches is provided by continuum Schwinger function methods (CSMs) [20–25]. In this framework, one typically works with QCD's Euler-Lagrange equations of motion – the Dyson-Schwinger equations (DSEs) – and develops symmetry preserving truncation schemes that enable a systematic connection to be made between each element of a given calculation and fields and/or terms in the QCD action. Regarding nucleon elastic electromagnetic form factors, two complementary paths are currently in use. Namely, a direct approach based on a 3-body Faddeev equation for the nucleon wave function [26, 27] and a quark + fully-interacting diquark - q(qq) - picture of nucleon structure [28, 29]. Both schemes are Poincarécovariant and can deliver form factors that cover and reach beyond the range of existing experiments.

One particular use of nucleon electromagnetic form factors is to produce charts of the distribution of charge and magnetisation within these states. Drawing analogies with nonrelativistic systems, three-dimensional Fourier transforms of the Poincaré-invariant Sachs electric and magnetic form factors [30], viz. $G_{E,M}^N(Q^2)$, when interpreted in the Breit frame, were long imagined to describe nucleon configuration space charge and magnetisation densities. However, this interpretation overlooks the fact that Poincaré-covariant wave functions do not

^{*} z.vao@hzdr.de

[†] cdroberts@nju.edu.cn

[‡] jose.rodriguez@dfaie.uhu.es

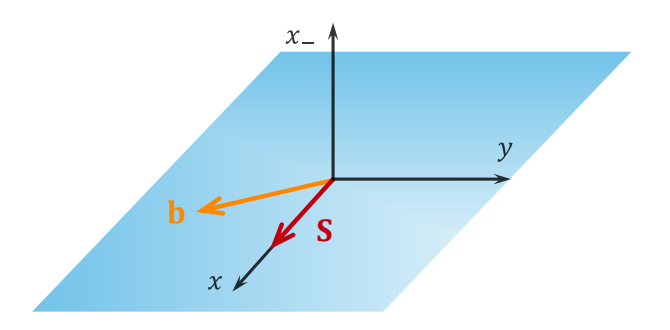


FIG. 1. With the nucleon's direction of motion defining the longitudinal light-front vector, the light-front transverse plane can be characterised by the usual two cartesian vectors, (\hat{x}, \hat{y}) , as marked by the blue surface in the image. The transverse position vector is indicated by \vec{b} – orange; and the transverse spin vector by \vec{S} – red.

have a probability interpretation; hence, cannot be used to define densities.

A contemporary alternative [31] considers projections of the Poincaré-invariant form factors onto the light-front via two-dimensional Fourier transforms with Q^2 interpreted in a Drell-Yan-West frame [32, 33]. Such functions describe true densities in a plane perpendicular to the light-front vector used in defining the nucleon state; see Fig. 1. Interpreted in the infinite momentum frame, this is the nucleon's direction of motion. No information is available about light-front-longitudinal charge and magnetisation distributions.

Herein, we calculate and compare transverse charge densities obtained using both the 3-body [27] and q(qq) [29] approaches to nucleon structure. Sections II and III provide a detailed discussion of the contemporary 3-body framework for calculation of nucleon form factors. This scheme was employed in Ref. [27], but little in the way of explanation was provided. A complete exposition of the modern q(qq) approach was provided in Ref. [29], so no recapitulation is necessary. Transverse charge and magnetisation densities, and the kindred charge density associated with a transversely polarised nucleon, are defined, and the CSM predictions reported and discussed in Sec. IV. Section V provides a summary and perspective.

II. FADDEEV EQUATION

A. Basic elements

Herein, we work at leading-order in a systematically-improvable, symmetry-preserving truncation of all quantum field (Dyson-Schwinger) equations which appear in the matrix element that defines the photon + nucleon interaction; namely, the rainbow-ladder (RL) truncation [34, 35]. It is worth mentioning here that, after roughly thirty years of use, RL truncation is known to be reliable for pion, kaon, and nucleon observables: (a) practically,

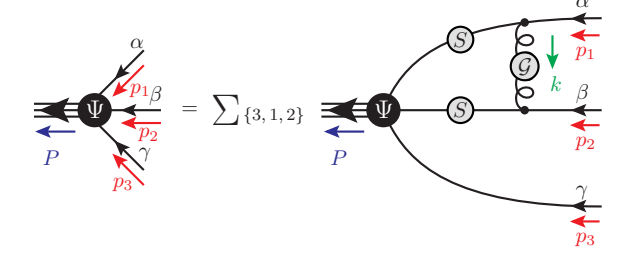


FIG. 2. Faddeev equation in RL truncation. Filled circle: Faddeev amplitude, Ψ , the matrix-valued solution, which involves 128 independent scalar functions. Spring: dressed-gluon interaction that mediates quark+quark scattering; see Eqs. (1), (2). Solid line: dressed-quark propagator, S, calculated from the rainbow gap equation. Lines not adorned with a shaded circle are amputated. Isospin symmetry is assumed. The sum runs over each of the cases involving quark "i=1,2,3" as a spectator to the exchange interaction.

owing to numerous successful applications [23, 36, 37]; and (b) because improvement schemes exist and have been tested, showing that the cumulative effect of improvements to RL truncation in these channels can be absorbed into a modest modification of the quark + quark scattering kernel [38–45]. Importantly, where reasonable comparisons are possible, modern CSM predictions and contemporary lattice-QCD results are mutually consistent – see, e.g., Refs. [22–24, 36, 37, 46–51].

In RL truncation, the nucleon bound state amplitude can be obtained by solving the Faddeev equation sketched in Fig. 2. Two elements are required to complete the definition of the Faddeev equation: (i) the quark + quark interaction, $\tilde{\mathcal{G}}$; and (ii) the dressed quark Schwinger function (propagator), S.

In RL truncation, the scattering kernel is obtained by writing [52]:

$$\mathcal{G}_{CD}^{AB}(k) = \tilde{\mathcal{G}}(y)[i\gamma_{\mu}\frac{\lambda^{a}}{2}]_{CB}[i\gamma_{\nu}\frac{\lambda^{a}}{2}]_{DA}T_{\mu\nu}^{k}, \qquad (1)$$

 $k^2T_{\mu\nu}^k=k^2\delta_{\mu\nu}-k_{\mu}k_{\nu},\ y=k^2,\ A,B,C,D$ represent colour and spinor matrix indices. The $T_{\mu\nu}$ specifies Landau gauge, employed because it is a fixed point of the renormalisation group and also that gauge for which corrections to RL truncation are least significant [53].

A realistic form of $\mathcal{G}_{\mu\nu}(y)$ is described in Refs. [41, 54]. It is specified by writing

$$\tilde{\mathcal{G}}(y) = \frac{8\pi^2}{\omega^4} De^{-y/\omega^2} + \frac{8\pi^2 \gamma_m \mathcal{F}(y)}{\ln\left[\tau + (1 + y/\Lambda_{\text{OCD}}^2)^2\right]}, \quad (2)$$

where $\gamma_m = 12/25$, $\Lambda_{\rm QCD} = 0.234\,{\rm GeV}$, $\tau = {\rm e}^2 - 1$, and $\mathcal{F}(y) = \{1 - \exp(-y/\Lambda_I^2)\}/y$, $\Lambda_I = 1\,{\rm GeV}$. We use a mass-independent (chiral-limit) momentum-subtraction renormalisation scheme [55], with renormalisation scale $\zeta = \zeta_{19} = 19\,{\rm GeV}$, viz. a far ultraviolet value so as to avoid truncation ambiguity and ensure that the the quark wave function renormalisation constant is essentially unity.

Numerous applications have revealed [23] that interactions in the class containing Eqs. (1), (2) can serve to unify the properties of many systems. Contemporary studies employ $\omega = 0.8\,\mathrm{GeV}$ [45]. Then, with $\omega D = 0.8\,\mathrm{GeV}^3$ and renormalisation point invariant quark current mass $\hat{m}_u = \hat{m}_d = 6.04\,\mathrm{MeV}$, which corresponds to a one-loop evolved mass at $\zeta = 2\,\mathrm{GeV}$ of 4.19 MeV, the following predictions are obtained: pion mass $m_\pi = 0.14\,\mathrm{GeV}$; nucleon mass $m_N = 0.94\,\mathrm{GeV}$; and pion leptonic decay constant $f_\pi = 0.094\,\mathrm{GeV}$. These values are a good match with experiment [56]. When the product ωD is held constant, physical observables remain practically unchanged under $\omega \to (1 \pm 0.2)\omega$ [57].

It is worth highlighting that all results obtained subsequently are parameter-free predictions. The interaction involves one parameter and there is a single quark current-mass. At this point, both quantities are fixed.

Here, it is also worth providing additional information about the interaction in Eq. (2). For instance, following Ref. [54], one may draw a connection between $\tilde{\mathcal{G}}$ and QCD's process-independent (PI) effective charge [58–60]. That PI charge is characterised by an infrared coupling value $\hat{\alpha}(0)/\pi = 0.97(4)$ and a gluon mass-scale $\hat{m}_0 = 0.43(1)$ GeV, both determined together via a combined continuum and lattice analysis of QCD's gauge sector [58]. The following values are those of analogous quantities inferred from Eq. (2):

$$\alpha_G(0)/\pi = 1.45$$
, $m_G = 0.54 \,\text{GeV}$. (3)

They agree fairly well with the QCD values.

Element (ii) in Fig. (2) is the dressed quark propagator, which has the form

$$S(k;\zeta) = Z(k^2;\zeta)/[i \cdot k + M(k^2)], \qquad (4)$$

where Z is the quark wave function renormalisation function and M is the renormalisation group invariant quark mass function. Herein, as required by symmetry considerations, it is obtained by solving the RL truncation quark gap (Dyson) equation. In accomplishing that task, we follow the procedures explained in Refs. [52, 61, 62].

B. Faddeev Amplitude

The solution of the three valence body equation sketched in Fig. 2 has the following form:

$$\Psi_{AB}^{CD}(p,q,P) = \sum_{i=1}^{3} \Psi_{ABCD}^{(i)}(p,q,P), \qquad (5)$$

where

$$\Psi_{ABCD}^{(1)}(p,q,P) = \int_{dk} \mathcal{G}_{BC}^{C'B'}(k) S_{B'B''}(k_2) S_{C'C''}(\tilde{k}_3)
\times \Psi_{AB''}^{C''D}(p^{(1)}, q^{(1)}, P),$$
(6a)
$$\Psi_{ABCD}^{(2)}(p,q,P) = \int_{dk} \mathcal{G}_{CA}^{A'C'}(k) S_{C'C''}(k_3) S_{A'A''}(\tilde{k}_1)$$

$$\times \Psi_{A''B}^{C''D}(p^{(2)}, q^{(2)}, P), \qquad (6b)$$

$$\Psi_{ABCD}^{(3)}(p, q, P) = \int_{dk} \mathcal{G}_{A'B'}^{B'A'}(k) S_{A'A''}(k_1) S_{B'B''}(\tilde{k}_2)$$

$$\times \Psi_{A''B''}^{CD}(p^{(3)}, q^{(3)}, P). \qquad (6c)$$

In Eq. (6), \int_{dk} represents a translationally invariant regularisation of the four-dimensional momentum-space integral and we have extended the range of the indices A, B, C, D to include spinor $(\alpha, \beta, \gamma, \delta)$, colour (r, s, t, u), and flavour (a, b, c, d), with D labelling these quantities for the nucleon itself.

Three independent particle momenta are involved in Eq. (6): p_1 , p_2 , p_3 . Momentum conservation requires $p_1 + p_2 + p_3 = P$, the total nucleon momentum. The other two (relative) momenta can be chosen in any way one desires; however, if one wishes to capitalise on permutation symmetry, then the following choices are best [26]:

$$p = (1 - \xi)p_3 - \xi (p_1 + p_2); \quad p_1 = -q - \frac{p}{2} + \frac{1 - \xi}{2}P,$$

$$q = \frac{p_2 - p_1}{2}; \qquad p_2 = q - \frac{p}{2} + \frac{1 - \xi}{2}P,$$

$$P = p_1 + p_2 + p_3; \qquad p_3 = p + \xi P, \qquad (7)$$

with $\xi=1/3$ being a momentum partitioning parameter. (We have verified that the results are independent of this choice, but the chosen value speeds the calculations.) The internal quark propagators depend on the quark momenta $k_i=p_i-k$ and $\tilde{k}_i=p_i+k$, with k being the exchanged momentum. For each of the three terms in Eq. (6), the internal relative momenta are:

$$p^{(1)} = p + k$$
, $p^{(2)} = p - k$, $p^{(3)} = p$,
 $q^{(1)} = q - k/2$, $q^{(2)} = q - k/2$, $q^{(3)} = q + k$. (8)

Owing to the spin, flavour, and colour structure of the nucleon, the Faddeev amplitude in Eqs. (5), (6) can be decomposed as follows:

$$\Psi_{AB}^{CD}(p,q,P) = \frac{\epsilon_{rst}}{\sqrt{6}} \otimes \sum_{\rho=0}^{1} \psi_{\alpha\beta\gamma}^{\rho \mathcal{I}}(p,q,P) \otimes \mathcal{F}_{abcd}^{\rho}, \quad (9)$$

where ϵ_{rst} expresses the antisymmetry of the nucleon amplitude under interchange of any two dressed-quark constituents, so the overall nucleon colour label is u = 0.

Some additional information is useful when discussing the isospin structure. The flavour amplitude is represented in an isospin basis spanned by the mixed–antisymmetric (MA) and mixed–symmetric (MS) flavour combinations, rather than directly in the proton–neutron basis. The corresponding flavour tensors are:

MA:
$$F_{abcd}^0 = \frac{1}{\sqrt{2}} i \left[\sigma_2\right]_{ab} \left[\mathbb{I}\right]_{cd}$$
, (10a)

MS:
$$F_{abcd}^1 = -\frac{1}{\sqrt{6}} \left[\sigma_j i \sigma_2 \right]_{ab} \left[\sigma_j \right]_{cd},$$
 (10b)

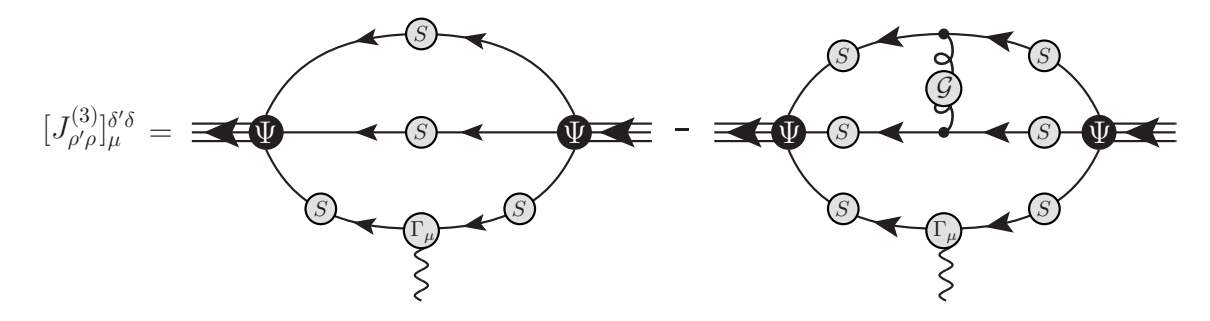


FIG. 3. The nucleon has three valence quarks, so the complete RL nucleon electromagnetic current has three terms: $J_{\mu}(Q) = \sum_{a=1,2,3} J_{\mu}^{a}(Q)$. Using symmetries, one can readily obtain the a=1,2 components once the a=3 component is known [63, Appendix B]. δ , δ' are spinor indices and ρ , ρ' are isospin indices. Γ_{μ} is the dressed-photon+quark vertex, which can be obtained, e.g., following Ref. [64].

where $\{\sigma_i, i = 1, 2, 3\}$ are the Pauli matrices and $[\mathbb{I} = \text{diag}[1, 1]$. In Eq. (10), under $a \leftrightarrow b$, the MA term is antisymmetric and MS is symmetric. Interpreted in terms of potential diquark correlations [28], MA corresponds to the isoscalar-scalar channel and MS to isovecoraxial vector.

The remaining piece in Eq. (9) is $\psi_{\alpha\beta\gamma}^{\rho\mathcal{I}}$, the momentumspin component, with \mathcal{I} recording the spin of the nucleon and $\rho = 0, 1$ ranging over MA, MS. By introducing an orthonormal set of 64 Dirac matrix valued tensors [65, Table 2], $\{X_{\alpha\beta\gamma\mathcal{I}}^{j}(p,q,P)\}$,

$$\frac{1}{4} \operatorname{tr} \left[\overline{\mathsf{X}}_{\beta \alpha \delta \gamma}^{i} \mathsf{X}_{\alpha \beta \gamma \delta}^{j} \right] = \delta_{ij} , \qquad (11)$$

this element may be decomposed into invariants as follows:

$$\psi_{\alpha\beta\gamma}^{\rho\mathcal{I}}(p,q,P) := \sum_{i=1}^{64} f^{i\rho}(p^2, q^2, z_0, z_1, z_2) \mathsf{X}_{\alpha\beta\gamma\mathcal{I}}^i, \quad (12)$$

where the expansion coefficients, f_i , are determined by solving the Faddeev equation and depend on five scalar variables, viz. with $\hat{p}^2 = 1$, $p_{\mu}^T = T_{\mu\nu}^P p_{\mu}$ etc.,

$$p^2$$
, q^2 , $z_0 = \hat{p}_T \cdot \hat{q}_T$, $z_1 = \hat{p} \cdot \hat{P}$, $z_2 = \hat{q} \cdot \hat{P}$. (13)

Now inserting Eqs. (1), (9) into Eq. (6c), one obtains

$$\psi_{\alpha\beta\gamma}^{\rho\mathcal{I}(3)}(p,q,P) = \frac{2}{3} \int_{k} \tilde{\mathcal{G}}(y) [\gamma_{\mu}]_{\alpha\alpha'} S_{\alpha'\alpha''}(k_{1}) [\gamma_{\nu}]_{\beta\beta'}$$
$$S_{\beta'\beta''}(\tilde{k}_{2}) T_{\mu\nu}(k) \psi_{\alpha''\beta''\gamma}^{\rho\mathcal{I}}(p^{(3)}, q^{(3)}, P). \tag{14}$$

Here, the colour and flavour projections have explicitly been completed, using

$$[F^{\rho'\dagger}]_{badc'}[F^{\rho}]_{abcd} = \delta_{\rho'\rho}\delta_{d'd'}. \tag{15}$$

Next, employing Eqs. (11), (12) in processing Eq. (14), one arrives at a system of equations for the 64×2 scalar functions $\{f_i^{\rho}\}$ that are required to fully characterise the solution of the Faddeev equation sketched in Fig. 2. Notably, the equations for the f^0 components are decoupled from those for f^1 , but the coupling reemerges when one uses permutation symmetry to reconstruct $\psi^{\rho}(1,2)$.

III. NUCLEON ELECTROMAGNETIC FORM FACTORS

The electromagnetic interaction current for a nucleon described by the solution of the Faddeev equation, Fig. 2, is obtained from the seven-point Schwinger function depicted in Fig. 3. For an on-shell nucleon, the general form of the current can be written as follows:

$$J_{\mu}^{N}(Q) = ie\Lambda_{+}(P_{f})[F_{1}^{N}(Q^{2})\gamma_{\mu} + \frac{1}{2m_{N}}\sigma_{\mu\nu}Q_{\nu}F_{2}^{N}(Q^{2})]\Lambda_{+}(P_{i}), \qquad (16)$$

where e is the positron charge, the incoming and outgoing nucleon momenta are $P_{i,f}$, $P = (P_f + P_i)/2$, $Q = P_f - P_i$, $P_{i,f}^2 = -m_N^2$, $\Lambda_+(P_{i,f})$ are positive-energy nucleonspinor projection operators, and $F_{1,2}^N$ are the Dirac and Pauli form factors.

Following Ref. [30], the nucleon charge and magnetisation distributions are normally defined as ($\tau = Q^2/[4m_N^2]$):

$$G_E^N = F_1^N - \tau F_2^N , \quad G_M^N = F_1^N + F_2^N .$$
 (17)

Magnetic moments and radii are calculated therefrom using standard definitions: $\mu_N = G_M^N(Q^2 = 0)$;

$$\langle r_F^2 \rangle^N = -6 \frac{d \ln G_F^N(Q^2)}{dQ^2} \bigg|_{Q^2=0} ,$$
 (18)

 $F=E,\ M,$ except $\langle r_E^2\rangle^n=-6G_E^{n\prime}(Q^2)|_{Q^2=0}$ because $G_E^n(0)=0.$

In working with the nucleon current in Fig. 3, we follow the computational procedure described in Ref. [63, Appendix B]. In that approach, the electromagnetic current is expressed in the form

$$J_{\mu}^{N}(Q) := \sum_{a=1}^{3} J_{\mu}^{aN}(Q) = \sum_{a=1}^{3} \sum_{\rho'\rho} \mathsf{F}_{\rho'\rho}^{(a)N} [J_{\rho'\rho}^{(a)N)}]_{\mu} \,. \quad (19)$$

Here, owing to permutation symmetries, it is sufficient to record

$$\mathsf{F}_{\rho'\rho}^{(3)N} = (e_N)_{d'} \, (F^{\rho'})_{bad'c'}^{\dagger} \, Q_{c'c} \, F_{abcd}^{\rho} \, (e_N)_d, \tag{20}$$

where $Q = \text{diag}[q_u = 2/3, q_d = -1/3]$ is the quark charge matrix associated with the photon + quark vertex, and $e_{N=p} = (1,0), e_{N=n} = (0,1)$ project onto the proton and neutron states, respectively. Studying Eq. (20), it becomes apparent that the four elements in $\{\mathsf{F}_{\rho'\rho}^{(3)N}\}$, labelled by $\{\rho', \rho\}$, are 2×2 matrices in isospin space.

The physical proton and neutron currents (hence, their form factors) are obtained by combining the $\rho=0,1$ contributions via the flavour matrices $\mathsf{F}^{(a)}_{\rho'\rho}$ in Eq. (19). Evaluating the expressions in Eq. (20), one finds:

$$\mathsf{F}^{(3)p} = \begin{pmatrix} \frac{2}{3} & 0\\ 0 & 0 \end{pmatrix}, \qquad \mathsf{F}^{(3)n} = \begin{pmatrix} -\frac{1}{3} & 0\\ 0 & \frac{1}{3} \end{pmatrix}. \tag{21}$$

It remains only to report the mathematical expression for the photon coupling to the quark in Fig. 3:

$$[J_{\rho'\rho}^{(3)}]_{\mu}^{\delta'\delta} = \int_{dpdq} \bar{\psi}_{\beta'\alpha'\gamma'}^{\rho'\delta'}(p_f, q_f, P_f) S_{\alpha'\alpha}(p_1) S_{\beta'\beta}(p_2)$$

$$\times [\chi_{\mu}(p_3, Q)]_{\gamma'\gamma} \left[\psi_{\alpha\beta\gamma}^{\rho\delta}(p_i, q_i, P_i) - \psi_{\alpha\beta\gamma}^{\rho\delta(3)}(p_i, q_i, P_i) \right],$$
(22)

where p_i, q_i and p_f, q_f are the incoming and outgoing relative momenta of the bound-state valence dressed quarks; P_i, P_f are the incoming, outgoing nucleon momenta; and $p_1, p_2, p_3^{\pm} = p_3 \pm Q/2$ are the quark momenta. For $\xi = 1/3$ in Eq. (7), one has

$$p_i = p - Q/3$$
, $p_f = p + Q/3$, $q_f = q_i = q$, (23a)

$$p_1 = -q - \frac{p}{2} + \frac{P}{3}, \quad p_2 = q - \frac{p}{2} + \frac{P}{3},$$
 (23b)

$$P_i = P - Q/2$$
, $P_f = P + Q/2$. (23c)

We note that Eq. (23c) merely specifies a Breit frame calculation; hence, is unconnected with the value of ξ .

Equation (22) also involves the unamputated photon + quark vertex, $\chi_{\mu}(p_3,Q) = S(p_3^+)\Gamma_{\mu}(p,Q)S(p_3^-)$, wherein the amputated vertex, $\Gamma_{\mu}(p,Q)$, is obtained as the solution of an inhomogeneous Bethe-Salpeter equation. This equation and its solution are discussed extensively elsewhere [64, 68].

Using Eqs. (19), (21) and permutation symmetry, one arrives at the following nucleon electromagnetic currents:

proton:
$$J_{\mu}^{\delta'\delta;p} = [2J_{00}^{(3)}]_{\mu}^{\delta'\delta},$$
 (24a)

neutron:
$$J_{\mu}^{\delta'\delta;n} = [J_{11}^{(3)} - J_{00}^{(3)}]_{\mu}^{\delta'\delta}$$
. (24b)

Referring to Eqs. (10), (20), then Eq. (24) means that there is no contribution to charged spin-half baryon form factors from MS pieces of the bound-state amplitude. A similar result is described elsewhere in the context of quark + diquark pictures of nucleon structure [69, Appendix C.1]: for such a baryon, "elastic" scattering from the axialvector diquark piece of its Faddeev wave functions does not contribute to its electromagnetic form factors.

The calculation described herein is made with reference to a hadron scale, $\zeta_{\mathcal{H}}$, whereat all properties of a given hadron are carried by its dressed valence degrees of freedom [70]. Hence, flavour-separated currents may be defined as follows:

u in proton:
$$2J_{\mu}^{p} + J_{\mu}^{n} = 3[J_{00}^{(3)}]_{\mu} + [J_{11}^{(3)}]_{\mu},$$
 (25a)

d in proton:
$$J^p_{\mu} + 2J^n_{\mu} = 2[J^{(3)}_{11}]_{\mu}$$
. (25b)

These results entail that the in-proton d-quark form factors receive no contribution from MA components of the proton Faddeev amplitude. Again, this has a long-known analogue in the quark + diquark picture of nucleon structure; namely, d quarks cannot be perceived by a hard probe unless axialvector diquark correlations are included in the proton Faddeev wave function [71–73].

With explicit expressions for the proton and neutron currents in hand, one can compute the associated Sachs form factors (the trace is over Dirac indices):

$$G_E^N(Q^2) = \frac{1}{2i\sqrt{1+\tau}} \operatorname{tr}\left[J_\mu^N \hat{P}_\mu\right], \qquad (26a)$$

$$G_M^N(Q^2) = \frac{i}{4\tau} \operatorname{tr} \left[J_\mu^N \gamma_\mu^T \right]. \tag{26b}$$

From these expressions, one readily obtains the nucleon Dirac and Pauli form factors via Eq. (17). The flavour-separated forms of these functions then follow from Eq. (25).

Canonical normalisation of the nucleon Faddeev amplitude is fixed by ensuring $G_E^p(0) = 1$. Current conservation, guaranteed by our formulation of the interaction current, is expressed in, amongst other things, the result $G_E^n(0) \equiv 0$.

IV. CHARGE AND MAGNETISATION DENSITIES

A. Transverse Dirac charge densities

Consider first nucleon transverse charge densities:

$$\rho_{ch}^{t}(|\vec{b}|) = \int \frac{d^{2}\Delta}{(2\pi)^{2}} e^{i\vec{b}\cdot\vec{\Delta}} F_{1}^{t}(\Delta^{2})$$
 (27a)

$$= \int_0^\infty \frac{d|\vec{\Delta}|}{2\pi} |\vec{\Delta}| J_0(|\vec{b}||\vec{\Delta}|) F_1^t(\Delta^2). \tag{27b}$$

Here, t = p, n, u, d, i.e., proton, neutron, u-quark, d-quark, with – see Eq. (25):

$$\rho_{ch}^{u}(|\vec{b}|) = 2\rho_{ch}^{p}(|\vec{b}|) + \rho_{ch}^{n}(|\vec{b}|), \qquad (28a)$$

$$\rho_{ch}^d(|\vec{b}|) = \rho_{ch}^p(|\vec{b}|) + 2\rho_{ch}^n(|\vec{b}|). \tag{28b}$$

Further, J_0 is a Bessel function of the first kind; $\vec{b} = (b_x, b_y) = |\vec{b}|(\cos \phi_b, \sin \phi_b)$; and $Q = (\vec{\Delta}, 0, 0)$.

Figure 4 depicts transverse charge densities for the proton and neutron. The primary theory curves, labelled

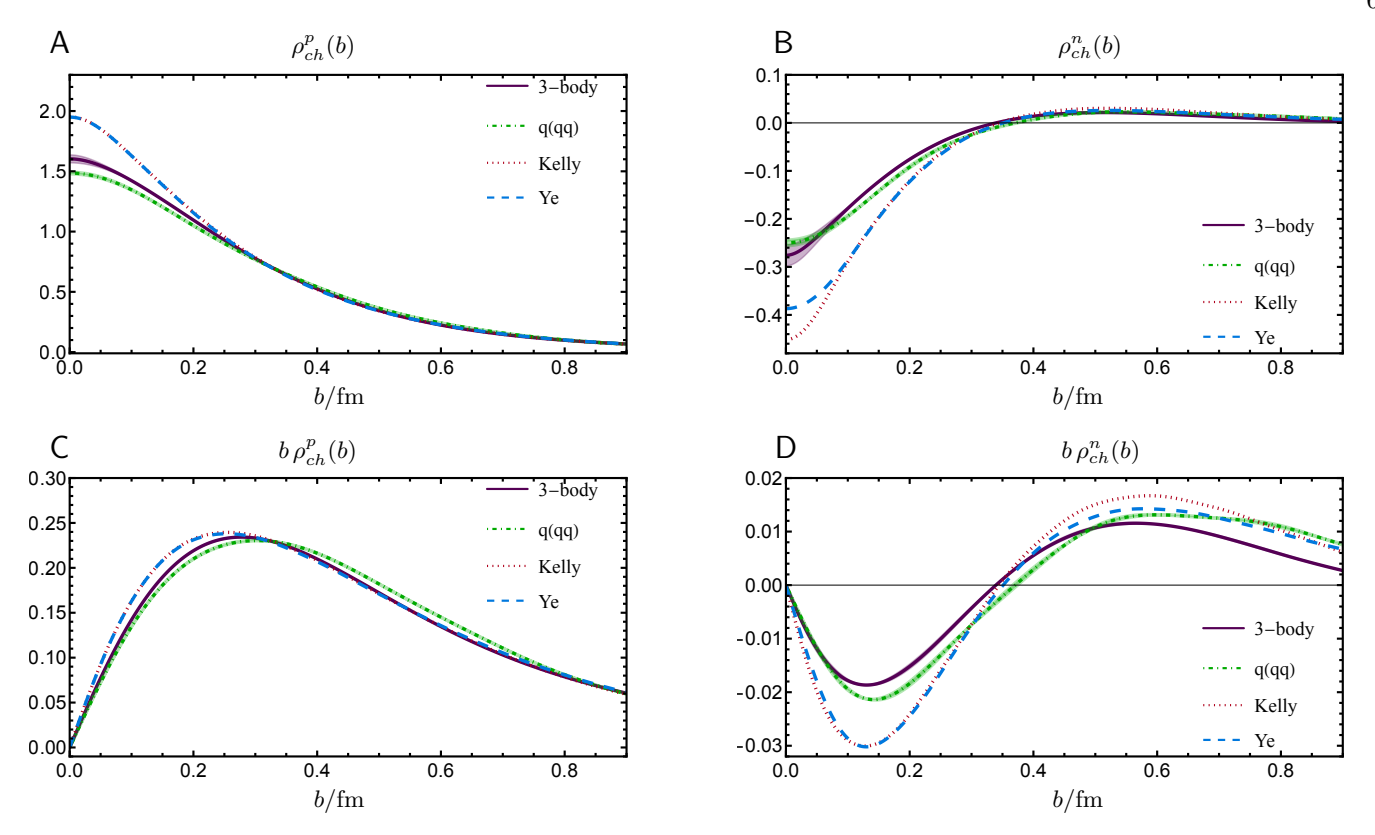


FIG. 4. Proton (p) and neutron (n) transverse charge densities. Panel A(B) $\rho_{ch}^{p(n)}$. Panel C(D) $b \rho_{ch}^{p(n)}$. Legend. Solid purple curve – density obtained from form factor calculated using three-body Faddeev equation and current [27], with, as therein, like-colour band indicating the associated uncertainty; dot-dashed green – density obtained using q(qq) form factor [29]; dashed blue – density from data parametrisation in Ref. [66, Ye]; and dotted red – from data parametrisation in Ref. [67, Kelly]. (Distributions plotted in units of fm⁻² and $b = |\vec{b}|$.))

"3-body", were obtained from the form factors reported in Ref. [27], which were calculated using the formalism described in Sects. II, III. These curves have an associated uncertainty. It expresses a 1σ -band deriving from the approach used to produce form factors at large- Δ^2 , namely, the Schlessinger point method (SPM) [74–76]. Details are provided in Ref. [27]: evidently, the impact on our results of this uncertainty is practically negligible. The second set of theory predictions was obtained using the quark + interacting-diquark, q(qq), picture of nucleon structure described in Ref. [29]. Those form factors are reported as functions of $x = Q^2/m_N^2$. To obtain results in GeV², we employed $m_N = 0.94$ GeV.

In all cases, there is fair agreement between the 3-body predictions and those obtained using q(qq) input. Moreover, both sets of predictions agree semiquantitatively with the results obtained using fits to data as input to Eq. (27). Those (modest) differences between theory and data-based inferences which are apparent might be connected with the omission of meson-baryon final state interactions (meson cloud effects) in the theoretical calculations employed herein. Further studies are needed before that can be confirmed.

The proton transverse charge density is positive definite on the entire $|\vec{b}|$ domain. Thus, one must expect

that at every point in the light-front transverse plane, the valence u-quark density exceeds the valence d-quark density.

On the other hand, the neutron transverse charge density is negative on a sizeable neighbourhood of the neutron's centre of transverse momentum (CoTM, $|\vec{b}| = 0$). It then becomes positive at $|\vec{b}| \approx 0.35\,\mathrm{fm}$ and remains so thereafter. These features were noted previously [77]. Mathematically, they are consequences of: (a) $F_1^n(\Delta^2 = 0) = 0$; (b) the non-positive character of $F_1^n(\Delta^2)$ and Δ^2 -dependent profile of this Dirac form factor, namely, in magnitude, with increasing Δ^2 , it rises to a maximum and then falls monotonically to zero; and (c) the oscillatory behaviour of the weight $|\vec{\Delta}| J_0(|\vec{b}||\vec{\Delta}|)$ at fixed $|\vec{b}|$.

In explanation, we note that, on $|\vec{b}| \simeq 0$, the $\rho^n_{ch}(|\vec{b}|)$ integrand is zero at $|\vec{\Delta}| = 0$, negative until its first zero, then oscillates with large steps between adjacent zeros and ever decreasing peak-height magnitudes; consequently, the value of the integral is dominated by the negative support at low $|\vec{\Delta}| = 0$, with all subsequent negative peaks giving larger negative contributions to the integral than the smaller positive peaks. As $|\vec{b}|$ increases, there comes a value at which the peak-height magnitude of the integrand's first positive peak exceeds that of the

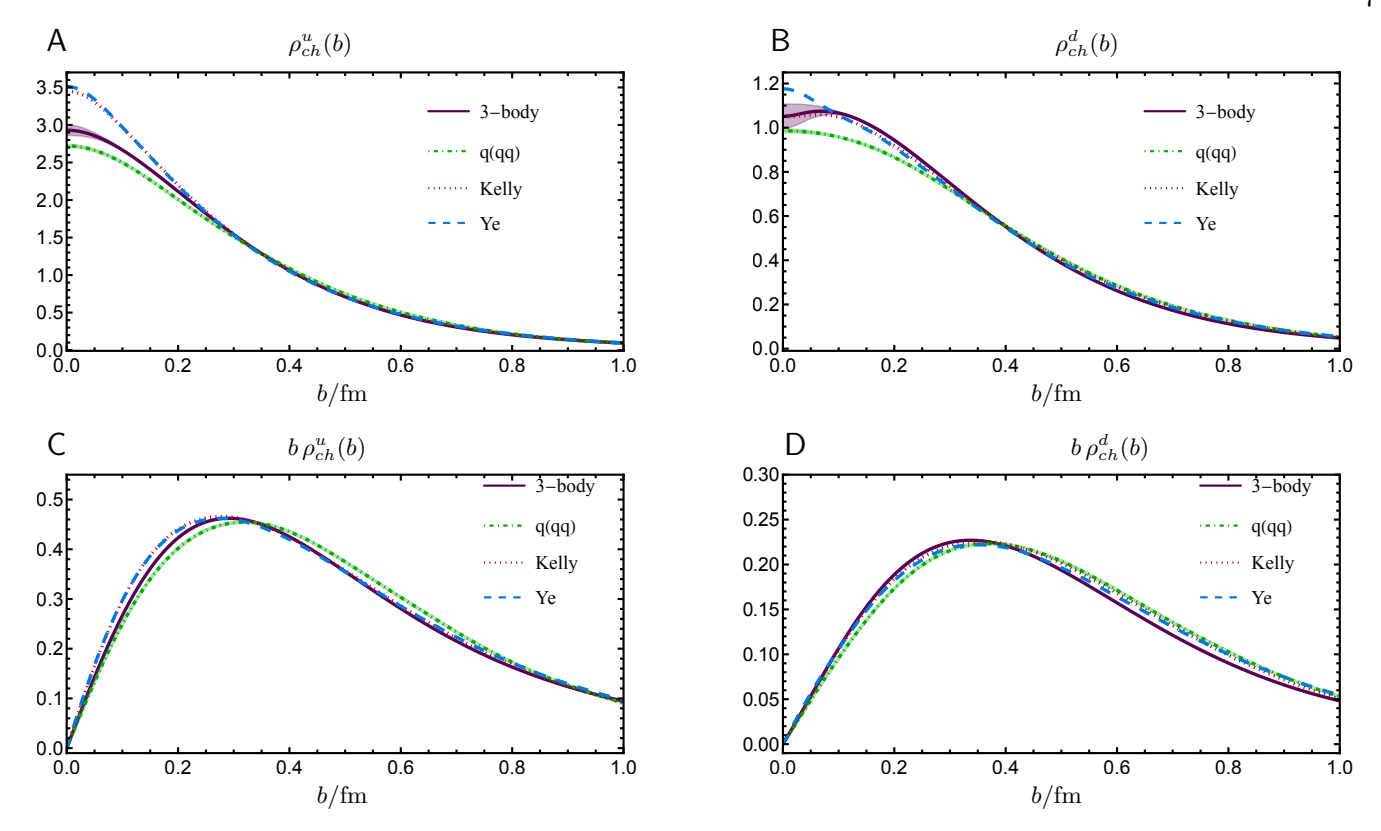


FIG. 5. u- and d-quark transverse charge densities. Panel A(B) $\rho_{ch}^{u(d)}$. Panel C(D) $b\,\rho_{ch}^{u(d)}$. Legend. Solid purple curve – density obtained from form factor calculated using three-body Faddeev equation and current [27], with, as therein, like-colour band indicating the associated uncertainty; dot-dashed green – density obtained using q(qq) form factor [29]; dashed blue – density from data parametrisation in Ref. [66, Ye]; and dotted red – from data parametrisation in Ref. [67, Kelly]. (Distributions plotted in units of fm⁻² and $b = |\vec{b}|$.)

first negative peak, which always occurs at a lower value of $|\vec{\Delta}|$. In this case, the positive contribution dominates on the domain bounded by the integrand's second nontrivial zero; and this pattern is repeated for all subsequent oscillations. Thus, the integral is positive. This pattern remains in effect thereafter, so $\rho_{ch}^n(|\vec{b}|)$ remains positive on $|\vec{b}| \gtrsim 0.35 \, \mathrm{fm}$.

Considering the above discussion, then one must expect that on $|\vec{b}| \lesssim 0.35 \,\mathrm{fm}$ in the light-front transverse plane, the *u*-quark density in the proton actually exceeds twice the *d*-quark density. This feature does not persist on the complementary domain; see, also, Ref. [77].

Having made this observation, transverse densities for the u- and d-quarks in the proton are displayed in Fig. 5. Evidently, the expectations described above are realised. Moreover, both in-proton valence-quark light-front transverse charge densities are positive definite.

To quantify some of the remarks made above, one may consider root-mean-square radii connected with the transverse-plane Dirac charge densities, viz. $\lambda_1^{u,d}$, where

$$(\lambda_1^{u,d})^2 := \frac{\int d^2 \vec{b} \, |\vec{b}|^2 \rho_1^{u,d}(|\vec{b}|)}{\int d^2 \vec{b} \, \rho_1^f(|\vec{b}|)}$$
$$= -4 \frac{d}{dQ^2} \ln F_1^{u,d}(Q^2) \bigg|_{Q^2 = 0}. \tag{29}$$

Predictions for these radii are compared with inferences from parametrisations of data in Table I. The 3-body transverse-plane Dirac radii are noticeably larger than those obtained using q(qq) input. Whilst not readily apparent in Fig. 5, this outcome owes to the 3-body den-

TABLE I. Theory predictions for in-proton valence-quark transverse density radii, defined via Eq. (29) with an obvious analogue for the magnetisation, in which the anomalous dressed valence-quark magnetic moment must be divided out. Inferences from data are also listed.

	$\lambda_1^u/{ m fm}$	λ_1^d/fm	$\lambda_2^u/{ m fm}$	$\lambda_2^d/{ m fm}$
3-body	0.68	0.69	0.63	0.68
q(qq)	0.53	0.57	0.62	0.67
[66, Ye]	0.66(1)	0.67(1)	0.71(12)	0.69(14)
[67, Kelly]	0.65	0.66	0.68	0.76

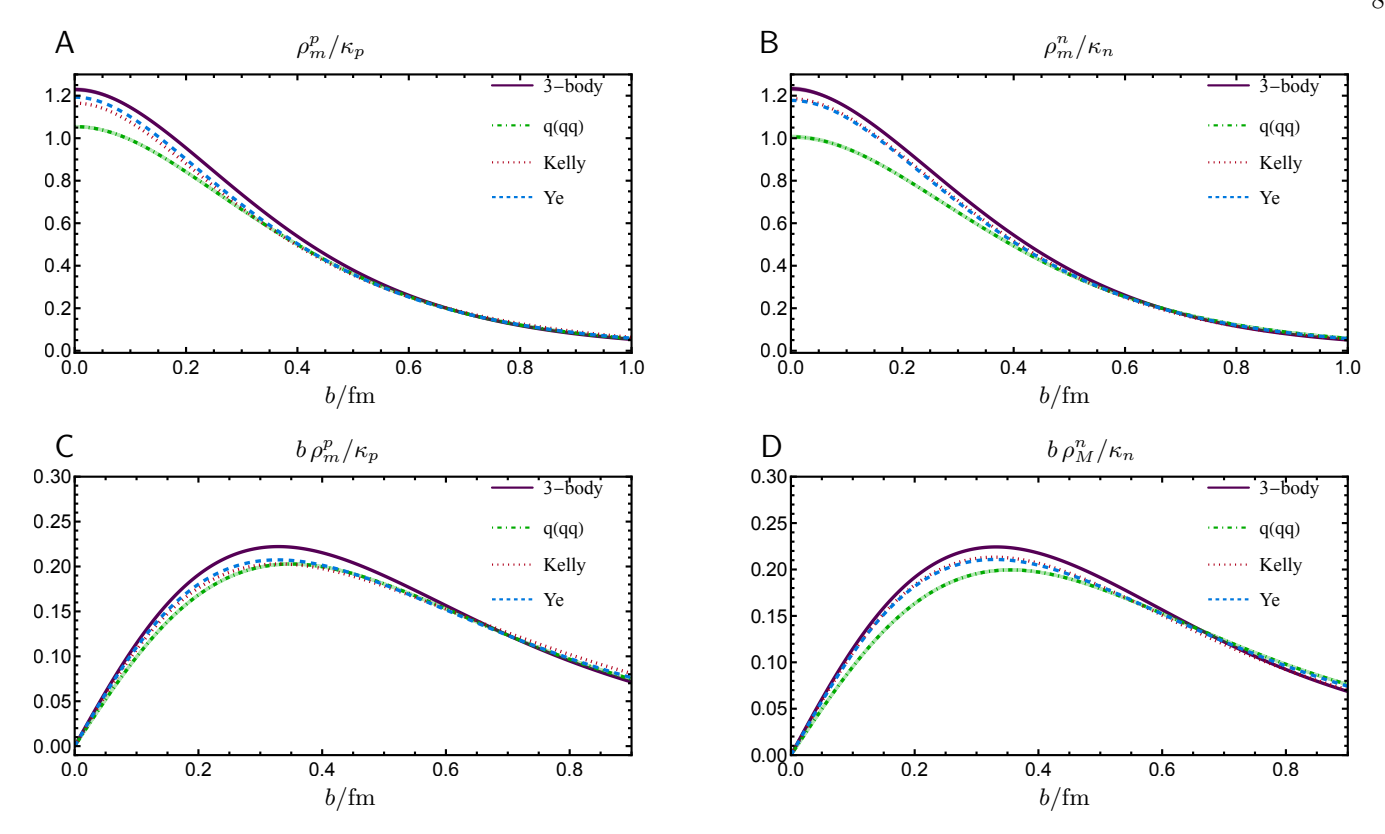


FIG. 6. Proton (p) and neutron (n) transverse magnetisation densities, Eq. (30). Panel A(B) $\rho_m^{p(n)}$. Panel C(D) $b \rho_m^{p(n)}$. Legend. Solid purple curve – density obtained from form factor calculated using three-body Faddeev equation and current [27], with, as therein, like-colour band indicating the associated uncertainty; dot-dashed green – density obtained using q(qq) form factor [29]; dashed blue – density from data parametrisation in Ref. [66, Ye]; and dotted red – from data parametrisation in Ref. [67, Kelly]. (Distributions plotted in units of fm⁻² and $b = |\vec{b}|$).)

sities having greater support on $|\vec{b}| \gtrsim 1.1\,\mathrm{fm}$. (Equally, referring to Ref. [29], the $Q^2 \simeq 0$ slope of the 3-body form factors is greater than that obtained in the q(qq) approach.) Turning to a comparison with inferences from data – see Table I, the 3-body predictions are in better agreement. Overall, we judge that the valence u- and d-quark transverse-plane Dirac radii are practically indistinguishable.

B. Transverse Pauli magnetisation densities

By analogy with Eq. (27), one may define light-front transverse magnetisation densities:

$$\rho_m^t(|\vec{b}|) = \int_0^\infty \frac{d|\vec{\Delta}|}{2\pi} |\vec{\Delta}| J_0(|\vec{b}||\vec{\Delta}|) F_2^t(\Delta^2).$$
 (30)

With this definition, one recovers the anomalous magnetic moments via:

$$\kappa^t = 2\pi \int_0^\infty d|\vec{b}| \, |\vec{b}| \, \rho_m^t(|\vec{b}|) \,. \tag{31}$$

Theory predictions for κ^t are compared with empirical determinations in Table II. The results obtained using the

3-body approach described above deliver underestimated values. As explained in Ref. [27], that is a failing of RL truncation, which yields a photon + quark vertex whose dressed-quark anomalous magnetic moment term is too small. This weakness is corrected in higher-order truncations [78]. Such corrections have been implemented in studies of mesons [45]. In future, it may be possible to adapt this scheme to baryons.

Transverse magnetisation densities for the proton and neutron are displayed in Fig. 6. In this case, all densities are positive definite; and the 3-body predictions agree best with empirical inferences (the anomalous magnetic moment has been divided out of $\rho_m^{p,n}$), although the q(qq) results are nonetheless a fair match.

The associated in-proton flavour-separated magnetisa-

TABLE II. Theory predictions for anomalous magnetic moments, κ in Eq. (31), compared with empirical determinations [56] and using Eq. (28), where necessary.

	κ_p	κ_n	κ_u	κ_d
Exp.	1.75	-1.91	1.59	-2.08
3-body	1.23	-1.33	1.13	-1.43
q(qq)	1.80	-1.86	1.74	-1.92

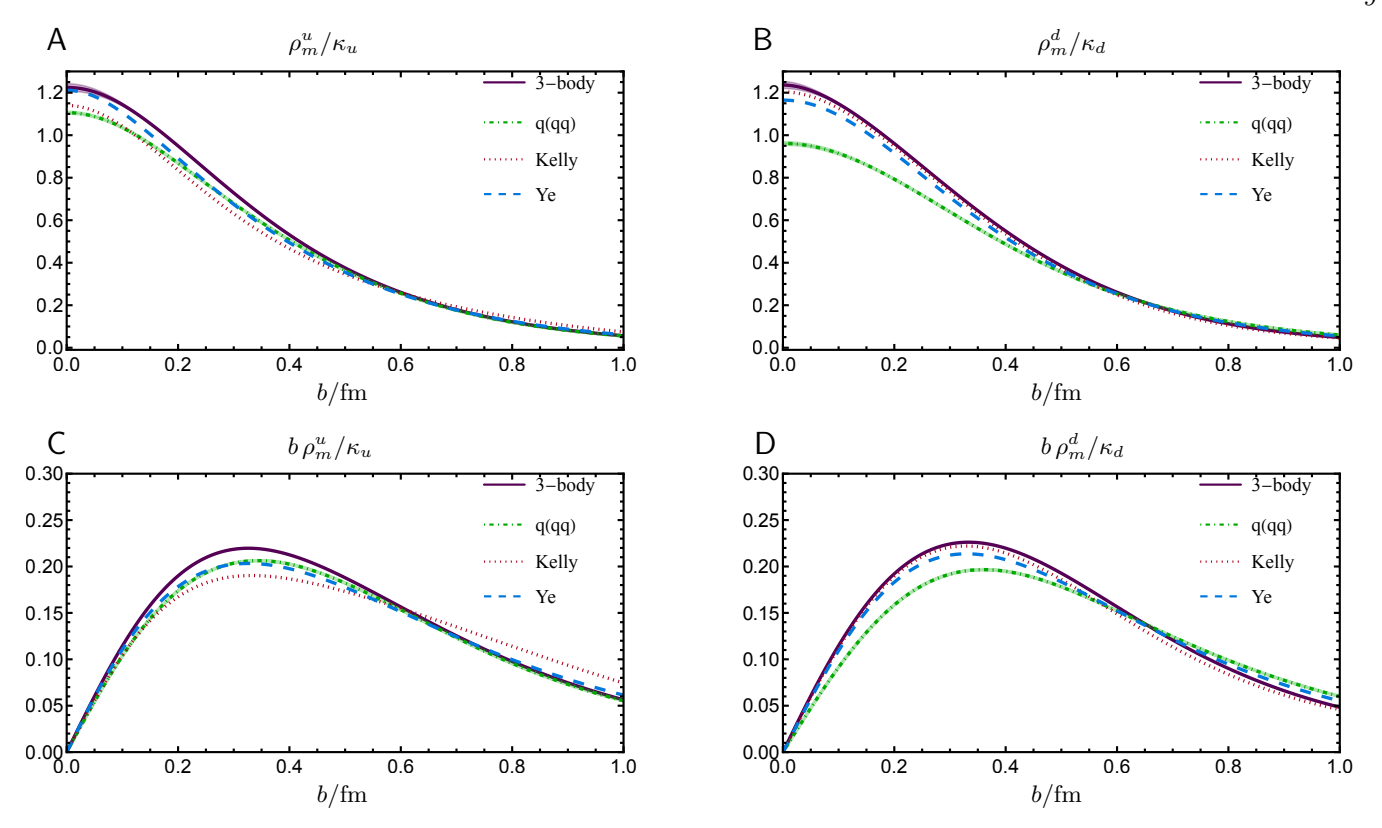


FIG. 7. u- and d-quark transverse magnetisation densities, Eq. (30). Panel A(B) $\rho_m^{u(d)}$. Panel C(D) $b \rho_m^{u(d)}$. Legend. Solid purple curve – density obtained from form factor calculated using three-body Faddeev equation and current [27], with, as therein, like-colour band indicating the associated uncertainty; dot-dashed green – density obtained using q(qq) form factor [29]; dashed blue – density from data parametrisation in Ref. [66, Ye]; and dotted red – from data parametrisation in Ref. [67, Kelly]. (Distributions plotted in units of fm⁻² and $b = |\vec{b}|$).)

tion densities are depicted in Fig. 7: owing to division by κ , each is positive definite. As observed elsewhere [29], the profiles in these panels highlight that the valence d-quark is magnetically very active within the proton: in magnitude, the d-quark profile is approximately equal (although opposite in sign) to the u-quark profile, even though the proton contains two valence u-quarks and only one d-quark. This outcome is correlated with suggestions from the q(qq) picture that, at $\zeta_{\mathcal{H}}$, the u valence quark angular momentum in the proton is much less than that of the d valence quark [50, 73, 79]. Furthermore, since, in a scalar diquark only proton, the dquark is locked within a magnetically inert [ud] correlation, the presence of axialvector diquarks in the proton is crucial to understanding ρ_m^u . Translated into the 3-body framework, this becomes a statement that MS components of the Faddeev wave function are important to obtain a valid description of in-proton valence d-quark behaviour.

Predictions for transverse-plane Pauli radii are recorded in Table I. Defined by analogy with Eq. (29), with the second line amended via normalisation by the $\kappa^{u,d}$ values, they are compared in the table with results inferred from fits to data. In this case, the 3-body and q(qq) predictions agree, with ordering that is consistent

with experimental inferences. Hence, one may conclude, that the in-proton transverse-plane valence d-quark Pauli radius is 9(2)% larger than the analogous valence u-quark radius.

C. Transverse charge densities for transversely polarised nucleon

For a nucleon prepared with polarisation transverse to its direction of motion, the light-front transverse charge density receives an additional contribution [80, 81]:

$$\rho_T(|\vec{b}|) = \rho_{\text{ch}}(|\vec{b}|) - \sin(\phi_b - \phi_s) \frac{1}{2m_N |\vec{b}|} \tilde{\rho}_m(|\vec{b}|), \quad (32)$$

where $\vec{S} = (\cos \phi_s, \sin \phi_s)$ is the nucleon polarisation unit-vector and

$$\tilde{\rho}_m^t(|\vec{b}|) = -|\vec{b}| \frac{\partial \rho_M^t(|\vec{b}|)}{\partial |\vec{b}|}$$
(33a)

$$= |\vec{b}| \int_0^\infty \frac{d|\vec{\Delta}|}{2\pi} \Delta^2 J_1(|\vec{\Delta}||\vec{b}|) F_2^t(\Delta^2). \tag{33b}$$

As illustrated in Fig. 1, associating the nucleon spin direction with the \hat{x} -axis ($\phi_s = 0$), then the light-front

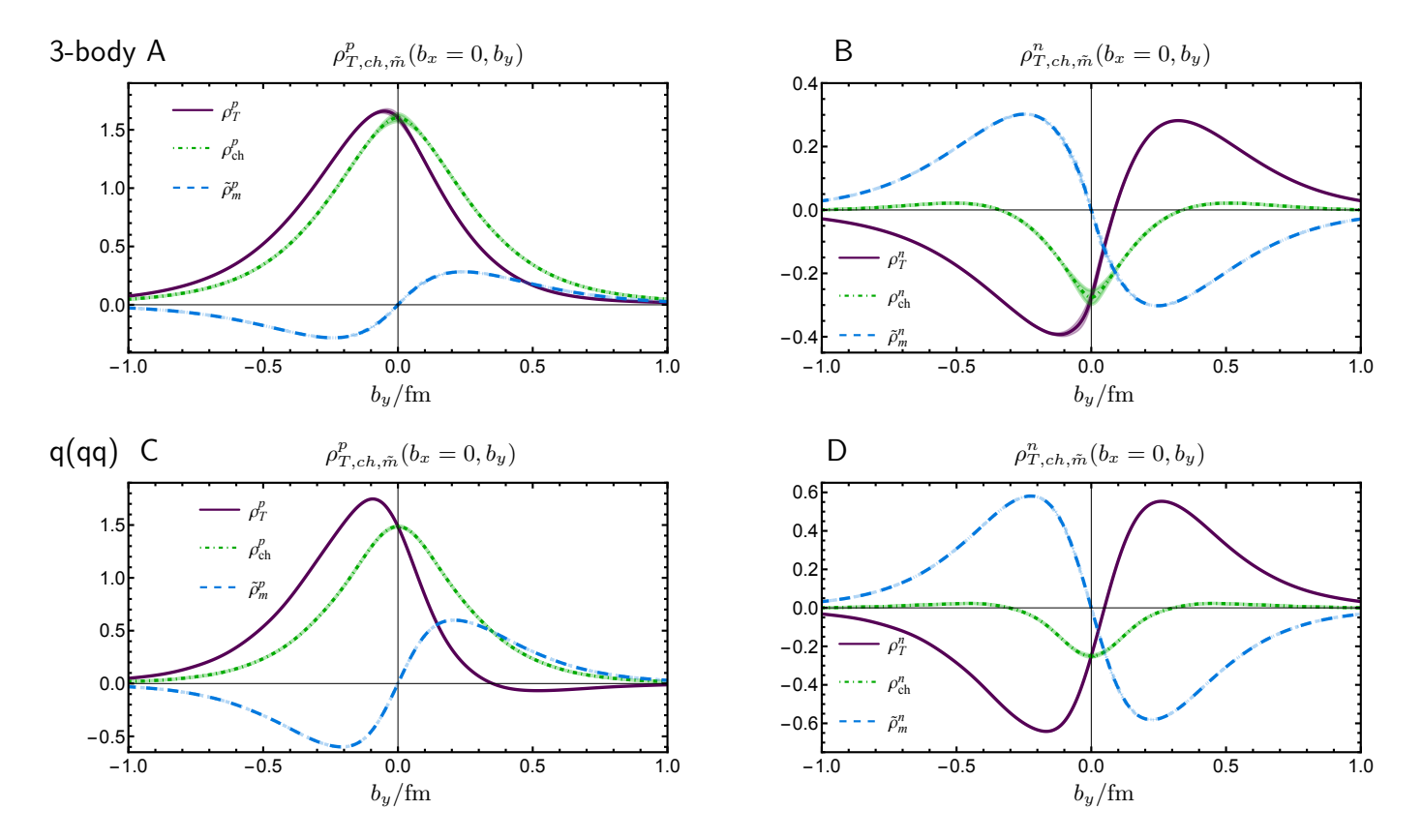


FIG. 8. All three proton and neutron light-front-transverse densities for a nucleon with transverse polarisation along \hat{y} . Panel A(B): $\rho^{p(n)}$ from three-body Faddeev equation [27]. Panel C(D): $\rho^{p(n)}$ from q(qq) treatment of nucleon [29]. Legend. Solid purple curve $-\rho_T^{p(n)}$; dot-dashed green $-\rho_{ch}^{p(n)}$; dashed blue $-\tilde{\rho}_m^{p(n)}$. Like coloured bands display SPM-related 1σ uncertainties. They are practically negligible. (Density distributions plotted in units of fm⁻²).

transverse charge density is distorted in the \hat{y} direction. On any domain for which $\tilde{\rho}_m^t(|\vec{b}|) > 0$, the shift is a reduction in $\rho_{\rm ch}(|\vec{b}|)$ on the positive \hat{y} axis $(\phi_b = \pi/2)$ and an increase on the negative \hat{y} axis.

The light-front transverse charge densities for a $+\hat{x}$ polarised nucleon are depicted in Fig. 8. The 3-body and q(qq) results are qualitatively and semi-quantitatively identical. For the polarised nucleons, there is a depletion of the charge density in the $+\hat{y}$ direction, with that strength shifted to the $-\hat{y}$ domain. This means that, in the presence of polarisation, the positive and negative charge densities are not symmetric around $b_y = 0$. Instead, positive charge is shifted to negative values of b_y and negative charge is shifted to positive b_y .

Flavour-separated images for a transversely polarised proton are displayed in Fig. 9. As anticipated above, on $-\hat{y}$, the u-quark densities are enhanced, whereas they are depleted on $+\hat{y}$. The reverse is true for the d-quark densities and the magnitude of the displacements is larger. The latter owes to the larger magnitude of κ_d – see Table II – which leads to a magnification of the shift generated by the second term in Eq. (32).

In Fig. 10, we draw two-dimensional density maps of the transverse charge densities for transversely polarised nucleons obtained using the 3-body approach. Based on the above discussion, those obtained in the q(qq) picture are qualitatively equivalent; so, we don't plot them. Supposing one is working in the infinite momentum frame, then these images depict a nucleon moving toward the observer. Plainly, the distribution is not rotationally symmetric around the proton direction of motion; instead, the positive charge density is distorted in the $-\hat{y}$ direction. Reflection symmetry through the \hat{y} axis is preserved. Although the effects for proton and neutron are similar, owing to its positive/negative character, the neutron's positive-charge density drift into the $-\hat{y}$ direction throughout the transverse plane is, perhaps, most noticeable.

V. SUMMARY AND PERSPECTIVE

Using input from 3-body and q(qq) Faddeev equation results for nucleon elastic electromagnetic form factors, we computed an array of light-front transverse densities for the proton and neutron and their dressed valencequark constituents, *i.e.*, flavour separations of the proton and neutron results. In completing such calculations, it

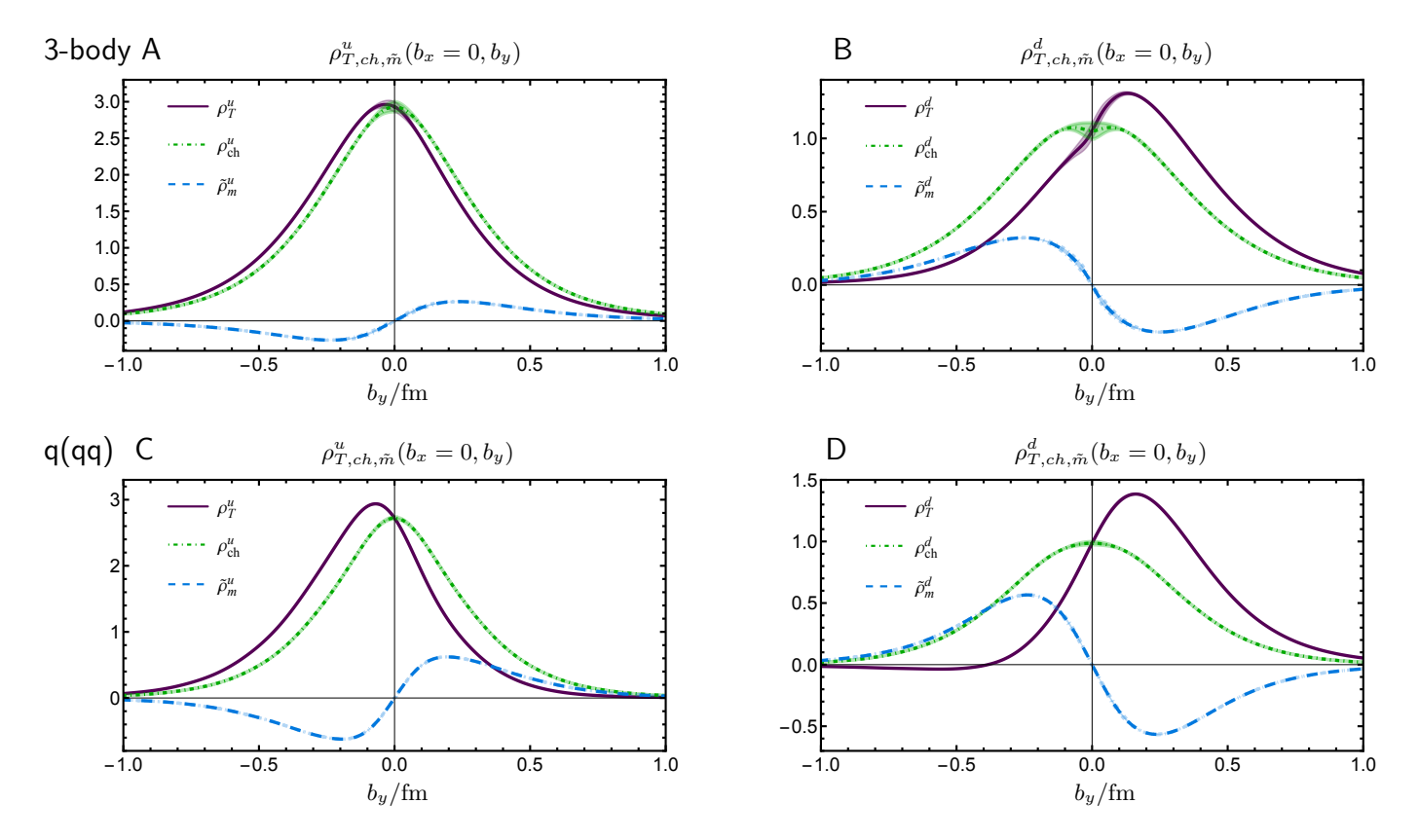


FIG. 9. Flavour separation of light-front-transverse densities for a proton with transverse polarisation along \hat{y} . Panel A(B): $\rho^{u(d)}$ from three-body Faddeev equation [27]. Panel C(D): $\rho^{u(d)}$ from q(qq) treatment of nucleon [29]. Legend. Solid purple curve $-\rho_T^{u(d)}$; dot-dashed green $-\rho_{ch}^{u(d)}$; dashed blue $-\tilde{\rho}_m^{u(d)}$. Once again, like coloured bands display SPM-related 1σ uncertainties. They are practically negligible. (Density distributions plotted in units of fm⁻²).

was crucial that both frameworks are Poincaré-covariant and deliver form factor predictions that extend to very large values of spacelike Q^2 . All results are collected and discussed in Sec. IV.

The key point is that the two complementary pictures of nucleon structure deliver predictions in qualitative and near-quantitative agreement, and that these predictions match expectations based on modern parametrisations of available data, where such are available. Underlying this success is the expression of emergent hadron mass (EHM) in the quark + quark interaction that drives both the 3-body and q(qq) results.

Looking to the future, one may anticipate a time at which lattice-QCD results reach a level of reliability that will allow quantitative comparisons with the full array of our predictions to be made. Given the common Schwinger function foundation of both continuum and lattice approaches, agreement would lend additional support to the EHM paradigm that underlies the continuum predictions.

On another track, the results presented herein could be extended to nucleon-to-resonance transition transverse densities. Such analyses are underway within the q(qq) framework. They will become possible in the 3-body approach once the Poincaré invariant transition form factors have been calculated, an effort which is in train.

ACKNOWLEDGMENTS

Work supported by: National Natural Science Foundation of China, grant no. 12135007; Natural Science Foundation of Anhui Province (grant no. 2408085QA028); Helmholtz-Zentrum Dresden-Rossendorf, under the High Potential Programme; Ministerio Español de Ciencia, Innovación y Universidades (MICINN) grant no. PID2022-140440NB-C22; and Junta de Andalucía contract nos. PAIDI FQM-370 and PCI+D+i under the title: "Tecnologías avanzadas para la exploración del universo y sus componentes" (Code AST22-0001).

R. Hofstadter, Electron scattering and nuclear structure, Rev. Mod. Phys. 28 (1956) 214–254.

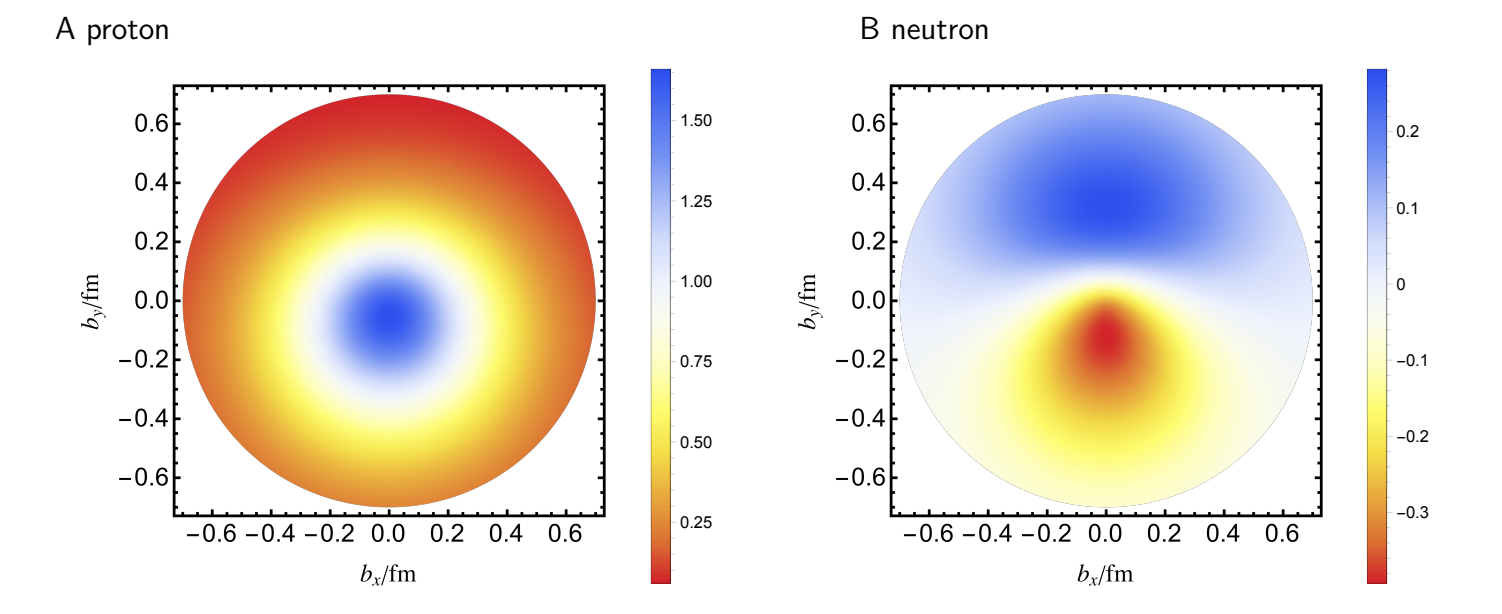


FIG. 10. With polarisation in the $+b_x$ direction, two-dimensional transverse charge densities of the proton (Panel A) and neutron (Panel B). Both results obtained using the 3-body framework. Images for the q(qq) picture are practically equivalent. (The unit of the density distribution is fm⁻².)

- electromagnetic form factors, Prog. Part. Nucl. Phys. 59 (2007) 694–764.
- [3] V. Punjabi, C. F. Perdrisat, M. K. Jones, E. J. Brash, C. E. Carlson, The Structure of the Nucleon: Elastic Electromagnetic Form Factors, Eur. Phys. J. A 51 (2015) 70
- [4] H. Gao, M. Vanderhaeghen, The proton charge radius, Rev. Mod. Phys. 94 (1) (2022) 015002.
- [5] Z.-F. Cui, D. Binosi, C. D. Roberts, S. M. Schmidt, Hadron and light nucleus radii from electron scattering, Chin. Phys. C 46 (12) (2022) 122001.
- [6] G. Gilfoyle, Future Measurements of the Nucleon Elastic Electromagnetic Form Factors at Jefferson Lab, EPJ Web Conf. 172 (2018) 02004.
- [7] B. Wojtsekhowski, Flavor Decomposition of Nucleon Form Factors – arXiv:2001.02190 [nucl-ex], 2020.
- [8] T. Yamazaki, Y. Aoki, T. Blum, H.-W. Lin, S. Ohta, S. Sasaki, R. Tweedie, J. Zanotti, Nucleon form factors with 2+1 flavor dynamical domain-wall fermions, Phys. Rev. D 79 (2009) 114505.
- [9] T. Bhattacharya, S. D. Cohen, R. Gupta, A. Joseph, H.-W. Lin, B. Yoon, Nucleon Charges and Electromagnetic Form Factors from 2+1+1-Flavor Lattice QCD, Phys. Rev. D 89 (9) (2014) 094502.
- [10] A. J. Chambers, et al., Electromagnetic form factors at large momenta from lattice QCD, Phys. Rev. D 96 (11) (2017) 114509.
- [11] C. Alexandrou, S. Bacchio, M. Constantinou, J. Finkenrath, K. Hadjiyiannakou, K. Jansen, G. Koutsou, A. Vaquero Aviles-Casco, Proton and neutron electromagnetic form factors from lattice QCD, Phys. Rev. D 100 (1) (2019) 014509.
- [12] C. Alexandrou, S. Bacchio, M. Constantinou, J. Finkenrath, K. Hadjiyiannakou, K. Jansen, G. Koutsou, G. Spanoudes, Nucleon electromagnetic form factors us-

- ing N_f =2+1+1 twisted mass fermion ensembles at the physical mass point, PoS LATTICE2022 (2023) 114.
- [13] S. Syritsyn, M. Engelhardt, S. Krieg, J. Negele, A. Pochinsky, Nucleon electromagnetic form factors at large momentum from Lattice QCD, PoS LATTICE2024 (2025) 340.
- [14] J. P. B. C. de Melo, T. Frederico, E. Pace, S. Pisano, G. Salme, Time- and Spacelike Nucleon Electromagnetic Form Factors beyond Relativistic Constituent Quark Models, Phys. Lett. B 671 (2009) 153–157.
- [15] M. M. Giannini, E. Santopinto, The hypercentral Constituent Quark Model and its application to baryon properties, Chin. J. Phys. 53 (2015) 020301.
- [16] R. S. Sufian, G. F. de Téramond, S. J. Brodsky, A. Deur, H. G. Dosch, Analysis of nucleon electromagnetic form factors from light-front holographic QCD: The spacelike region, Phys. Rev. D 95 (1) (2017) 014011.
- [17] C. Mondal, S. Xu, J. Lan, X. Zhao, Y. Li, D. Chakrabarti, J. P. Vary, Proton structure from a lightfront Hamiltonian, Phys. Rev. D 102 (1) (2020) 016008.
- [18] M. Ahmady, D. Chakrabarti, C. Mondal, R. Sandapen, Nucleon electroweak form factors using spin-improved holographic light-front wavefunctions, Nucl. Phys. A 1016 (2021) 122334.
- [19] S. Xu, C. Mondal, J. Lan, X. Zhao, Y. Li, J. P. Vary, Nucleon structure from basis light-front quantization, Phys. Rev. D 104 (9) (2021) 094036.
- [20] G. Eichmann, H. Sanchis-Alepuz, R. Williams, R. Alkofer, C. S. Fischer, Baryons as relativistic three-quark bound states, Prog. Part. Nucl. Phys. 91 (2016) 1–100.
- [21] V. D. Burkert, C. D. Roberts, Colloquium: Roper resonance: Toward a solution to the fifty-year puzzle, Rev. Mod. Phys. 91 (2019) 011003.
- [22] D. Binosi, Emergent Hadron Mass in Strong Dynamics,

- Few Body Syst. 63 (2) (2022) 42.
- [23] M. Ding, C. D. Roberts, S. M. Schmidt, Emergence of Hadron Mass and Structure, Particles 6 (1) (2023) 57– 120.
- [24] M. N. Ferreira, J. Papavassiliou, Gauge Sector Dynamics in QCD, Particles 6 (1) (2023) 312–363.
- [25] P. Achenbach, D. S. Carman, R. W. Gothe, K. Joo, V. I. Mokeev, C. D. Roberts, Electroexcitation of Nucleon Resonances and the Emergence of Hadron Mass, Symmetry 17 (7) (2025) 1106.
- [26] G. Eichmann, Nucleon electromagnetic form factors from the covariant Faddeev equation, Phys. Rev. D 84 (2011) 014014.
- [27] Z.-Q. Yao, D. Binosi, Z.-F. Cui, C. D. Roberts, Nucleon charge and magnetisation distributions: flavour separation and zeroes – arXiv:2403.08088 [hep-ph], Fund. Res. (2025) in press 10.1016/j.fmre.2024.11.005.
- [28] M. Y. Barabanov, et al., Diquark Correlations in Hadron Physics: Origin, Impact and Evidence, Prog. Part. Nucl. Phys. 116 (2021) 103835.
- [29] P. Cheng, Z. Q. Yao, D. Binosi, Y. Lu, C. D. Roberts, Quark + Diquark Description of Nucleon Elastic Electromagnetic Form Factors, Eur. Phys. J. A (2025) in press.
- [30] R. Sachs, High-Energy Behavior of Nucleon Electromagnetic Form Factors, Phys. Rev. 126 (1962) 2256–2260.
- [31] G. A. Miller, Transverse Charge Densities, Ann. Rev. Nucl. Part. Sci. 60 (2010) 1–25.
- [32] S. D. Drell, T.-M. Yan, Connection of Elastic Electromagnetic Nucleon Form-Factors at Large Q**2 and Deep Inelastic Structure Functions Near Threshold, Phys. Rev. Lett. 24 (1970) 181–185.
- [33] G. B. West, Phenomenological model for the electromagnetic structure of the proton, Phys. Rev. Lett. 24 (1970) 1206–1209.
- [34] H. J. Munczek, Dynamical chiral symmetry breaking, Goldstone's theorem and the consistency of the Schwinger-Dyson and Bethe-Salpeter Equations, Phys. Rev. D 52 (1995) 4736–4740.
- [35] A. Bender, C. D. Roberts, L. von Smekal, Goldstone Theorem and Diquark Confinement Beyond Rainbow- Ladder Approximation, Phys. Lett. B 380 (1996) 7–12.
- [36] C. D. Roberts, D. G. Richards, T. Horn, L. Chang, Insights into the emergence of mass from studies of pion and kaon structure, Prog. Part. Nucl. Phys. 120 (2021) 103883.
- [37] K. Raya, A. Bashir, D. Binosi, C. D. Roberts, J. Rodríguez-Quintero, Pseudoscalar Mesons and Emergent Mass, Few Body Syst. 65 (2) (2024) 60.
- [38] C. S. Fischer, R. Williams, Probing the gluon selfinteraction in light mesons, Phys. Rev. Lett. 103 (2009) 122001.
- [39] L. Chang, C. D. Roberts, Sketching the Bethe-Salpeter kernel, Phys. Rev. Lett. 103 (2009) 081601.
- [40] L. Chang, I. C. Cloet, J. J. Cobos-Martinez, C. D. Roberts, S. M. Schmidt, P. C. Tandy, Imaging dynamical chiral symmetry breaking: pion wave function on the light front, Phys. Rev. Lett. 110 (2013) 132001.
- [41] D. Binosi, L. Chang, J. Papavassiliou, C. D. Roberts, Bridging a gap between continuum-QCD and ab initio predictions of hadron observables, Phys. Lett. B 742 (2015) 183–188.
- [42] R. Williams, C. S. Fischer, W. Heupel, Light mesons in QCD and unquenching effects from the 3PI effective action, Phys. Rev. D 93 (2016) 034026.

- [43] D. Binosi, L. Chang, S.-X. Qin, J. Papavassiliou, C. D. Roberts, Symmetry preserving truncations of the gap and Bethe-Salpeter equations, Phys. Rev. D 93 (2016) 096010.
- [44] D. Binosi, L. Chang, J. Papavassiliou, S.-X. Qin, C. D. Roberts, Natural constraints on the gluon-quark vertex, Phys. Rev. D 95 (2017) 031501(R).
- [45] Z.-N. Xu, Z.-Q. Yao, S.-X. Qin, Z.-F. Cui, C. D. Roberts, Bethe-Salpeter kernel and properties of strange-quark mesons, Eur. Phys. J. A 59 (3) (2023) 39.
- [46] C. Chen, C. S. Fischer, C. D. Roberts, J. Segovia, Nucleon axial-vector and pseudoscalar form factors and PCAC relations, Phys. Rev. D 105 (9) (2022) 094022.
- [47] L. Chang, C. D. Roberts, Regarding the distribution of glue in the pion, Chin. Phys. Lett. 38 (8) (2021) 081101.
- [48] Y. Lu, Y.-Z. Xu, K. Raya, C. D. Roberts, J. Rodríguez-Quintero, Pion distribution functions from low-order Mellin moments, Phys. Lett. B 850 (2024) 138534.
- [49] C. Chen, C. S. Fischer, C. D. Roberts, Nucleon to Δ axial and pseudoscalar transition form factors, Phys. Rev. Lett. 133 (13) (2024) 131901.
- [50] Y. Yu, P. Cheng, H.-Y. Xing, F. Gao, C. D. Roberts, Contact interaction study of proton parton distributions, Eur. Phys. J. C 84 (7) (2024) 739.
- [51] C. Alexandrou, et al., Quark and Gluon Momentum Fractions in the Pion and in the Kaon, Phys. Rev. Lett. 134 (13) (2025) 131902.
- [52] P. Maris, C. D. Roberts, π and K meson Bethe-Salpeter amplitudes, Phys. Rev. C 56 (1997) 3369–3383.
- [53] A. Bashir, A. Raya, S. Sánchez-Madrigal, C. D. Roberts, Gauge invariance of a critical number of flavours in QED3, Few Body Syst. 46 (2009) 229–237.
- [54] S.-X. Qin, L. Chang, Y.-X. Liu, C. D. Roberts, D. J. Wilson, Interaction model for the gap equation, Phys. Rev. C 84 (2011) 042202(R).
- [55] L. Chang, Y.-X. Liu, C. D. Roberts, Y.-M. Shi, W.-M. Sun, H.-S. Zong, Chiral susceptibility and the scalar Ward identity, Phys. Rev. C 79 (2009) 035209.
- [56] S. Navas, et al., Review of particle physics, Phys. Rev. D 110 (3) (2024) 030001.
- [57] S.-X. Qin, C. D. Roberts, Impressions of the Continuum Bound State Problem in QCD, Chin. Phys. Lett. 37 (12) (2020) 121201.
- [58] Z.-F. Cui, J.-L. Zhang, D. Binosi, F. de Soto, C. Mezrag, J. Papavassiliou, C. D. Roberts, J. Rodríguez-Quintero, J. Segovia, S. Zafeiropoulos, Effective charge from lattice QCD, Chin. Phys. C 44 (2020) 083102.
- [59] A. Deur, S. J. Brodsky, C. D. Roberts, QCD Running Couplings and Effective Charges, Prog. Part. Nucl. Phys. 134 (2024) 104081.
- [60] S. J. Brodsky, A. Deur, C. D. Roberts, The Secret to the Strongest Force in the Universe, Sci. Am. 5 (May) (2024) 32–39.
- [61] P. Maris, P. C. Tandy, QCD modeling of hadron physics, Nucl. Phys. Proc. Suppl. 161 (2006) 136–152.
- [62] A. Krassnigg, Excited mesons in a Bethe-Salpeter approach, PoS CONFINEMENT 8 (2008) 075.
- [63] G. Eichmann, C. S. Fischer, Nucleon axial and pseudoscalar form factors from the covariant Faddeev equation, Eur. Phys. J. A 48 (2012) 9.
- [64] Y.-Z. Xu, D. Binosi, Z.-F. Cui, B.-L. Li, C. D. Roberts, S.-S. Xu, H.-S. Zong, Elastic electromagnetic form factors of vector mesons, Phys. Rev. D 100 (2019) 114038.
- [65] G. Eichmann, R. Alkofer, A. Krassnigg, D. Nicmorus,

- Covariant solution of the three-quark problem in quantum field theory: The Nucleon, EPJ Web Conf. 3 (2010) 03028.
- [66] Z. Ye, J. Arrington, R. J. Hill, G. Lee, Proton and Neutron Electromagnetic Form Factors and Uncertainties, Phys. Lett. B 777 (2018) 8–15.
- [67] J. J. Kelly, Simple parametrization of nucleon form factors, Phys. Rev. C 70 (2004) 068202.
- [68] Y.-Z. Xu, S. Chen, Z.-Q. Yao, D. Binosi, Z.-F. Cui, C. D. Roberts, Vector-meson production and vector meson dominance, Eur. Phys. J. C 81 (2021) 895.
- [69] D. J. Wilson, I. C. Cloet, L. Chang, C. D. Roberts, Nucleon and Roper electromagnetic elastic and transition form factors, Phys. Rev. C 85 (2012) 025205.
- [70] P.-L. Yin, Y.-Z. Xu, Z.-F. Cui, C. D. Roberts, J. Rodríguez-Quintero, All-Orders Evolution of Parton Distributions: Principle, Practice, and Predictions, Chin. Phys. Lett. Express 40 (9) (2023) 091201.
- [71] F. E. Close, A. W. Thomas, The Spin and Flavor Dependence of Parton Distribution Functions, Phys. Lett. B 212 (1988) 227.
- [72] Z.-F. Cui, F. Gao, D. Binosi, L. Chang, C. D. Roberts, S. M. Schmidt, Valence quark ratio in the proton, Chin. Phys. Lett. Express 39 (04) (2022) 041401.
- [73] P. Cheng, Y. Yu, H.-Y. Xing, C. Chen, Z.-F. Cui, C. D.

- Roberts, Perspective on polarised parton distribution functions and proton spin, Phys. Lett. B 844 (2023) 138074.
- [74] L. Schlessinger, C. Schwartz, Analyticity as a Useful Computation Tool, Phys. Rev. Lett. 16 (1966) 1173– 1174.
- [75] L. Schlessinger, Use of Analyticity in the Calculation of Nonrelativistic Scattering Amplitudes, Phys. Rev. 167 (1968) 1411–1423.
- [76] R. A. Tripolt, I. Haritan, J. Wambach, N. Moiseyev, Threshold energies and poles for hadron physical problems by a model-independent universal algorithm, Phys. Lett. B 774 (2017) 411–416.
- [77] G. A. Miller, Charge Density of the Neutron, Phys. Rev. Lett. 99 (2007) 112001.
- [78] L. Chang, Y.-X. Liu, C. D. Roberts, Dressed-quark anomalous magnetic moments, Phys. Rev. Lett. 106 (2011) 072001.
- [79] Y. Yu, C. D. Roberts, Impressions of Parton Distribution Functions, Chin. Phys. Lett. 41 (2024) 121202.
- [80] M. Burkardt, Impact parameter space interpretation for generalized parton distributions, Int. J. Mod. Phys. A 18 (2003) 173–208.
- [81] C. E. Carlson, M. Vanderhaeghen, Empirical transverse charge densities in the nucleon and the nucleon-to-Delta transition, Phys. Rev. Lett. 100 (2008) 032004.